Science Robotics
AAAS

Supplementary Materials for

High-performance electrified hydrogel actuators based on wrinkled nanomembrane electrodes for untethered insect-scale soft aquabots

Jongkuk Ko *et al.*

Corresponding author: Jinhan Cho, jinhan71@korea.ac.kr; Je-Sung Koh, jskoh@ajou.ac.kr

Sci. Robot. **7**, eabo6463 (2022)
DOI: 10.1126/scirobotics.abo6463

The PDF file includes:

Other Supplementary Material for this manuscript includes the following:

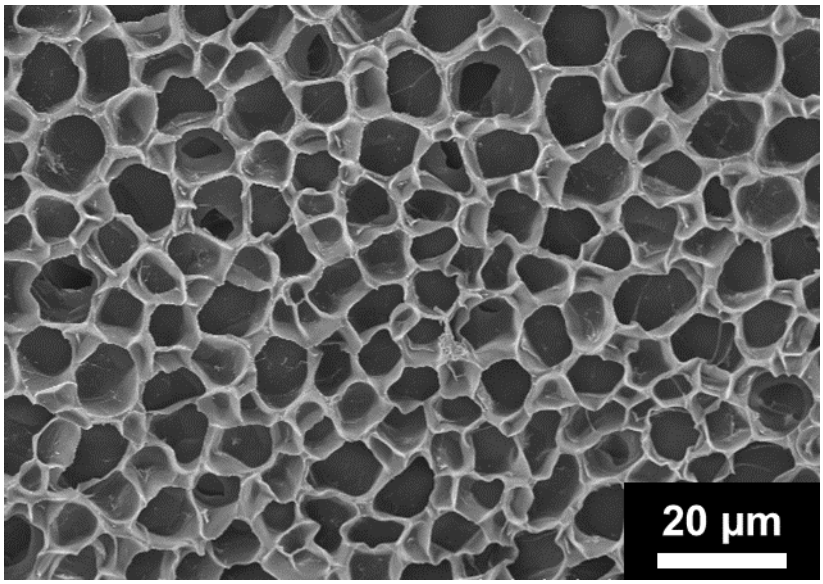

Figure S1. Porous structures of PAA-co-PAAm hydrogel. FE-SEM images of freeze dried PAA-co-PAAm hydrogel showing porous structures whose average size is about 10 µm

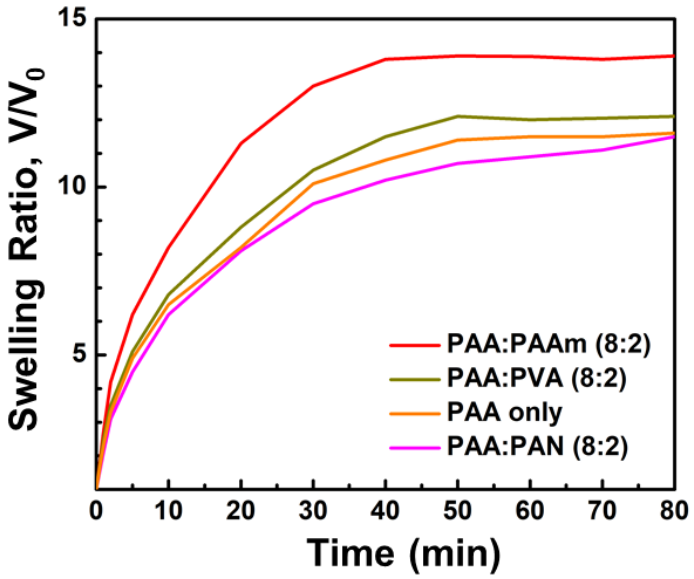

Figure S2. Swelling dynamics of hydrogels with different composition. Volume changes of acrylic acid-based hydrogels synthesized with different monomers in aqueous PEI solution (30 mg mL^{-1}). Volume of PEI-infiltrated hydrogels in dried states were used as initial volume of hydrogels (V_0). In this case, it was observed that the swelling ratio of PAA-co-PAAm hydrogel in aqueous PEI solution was much higher than those of other hydrogels including pure PAA hydrogel because of superior hydrophilicity of acrylamide groups, facilitating the incorporation and transport of water inside hydrogel matrix. That is, the favorable hydrogen-bonding/electrostatic interactions between COOH groups of PAA and NH_2 groups of PAAm as well as between COOH groups of PAA and NH_2 groups of PEI can induce the formation of polymeric network structure with slight crosslinking density, resulting in the notable increase of swelling ratio of hydrogel. The actuation performance depending on the chemical composition of hydrogels will be shown in fig. S18.

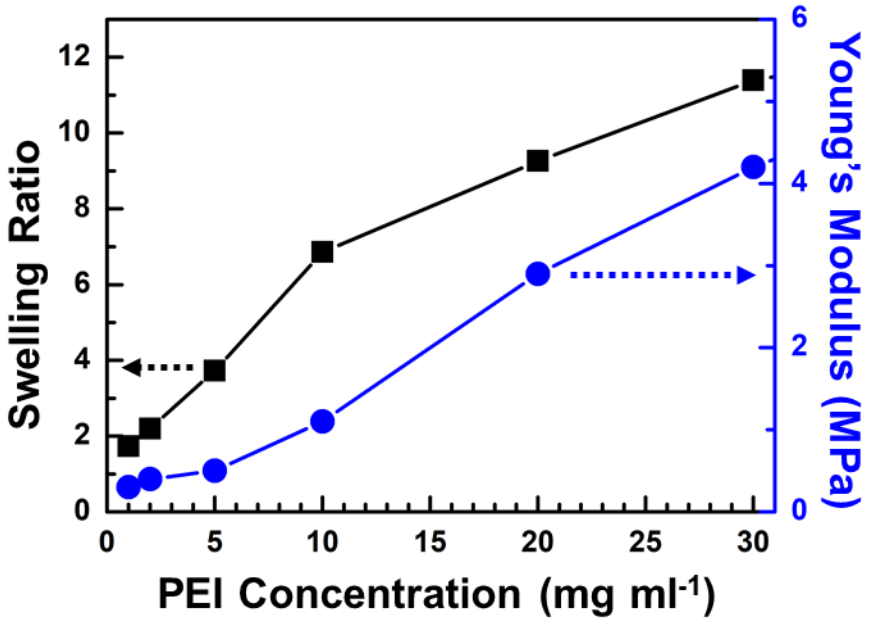

Figure S3. PEI concentration-dependent mechanical properties. PEI concentration-dependent swelling ratio and Young's modulus of PAA-co-PAAm hydrogels.

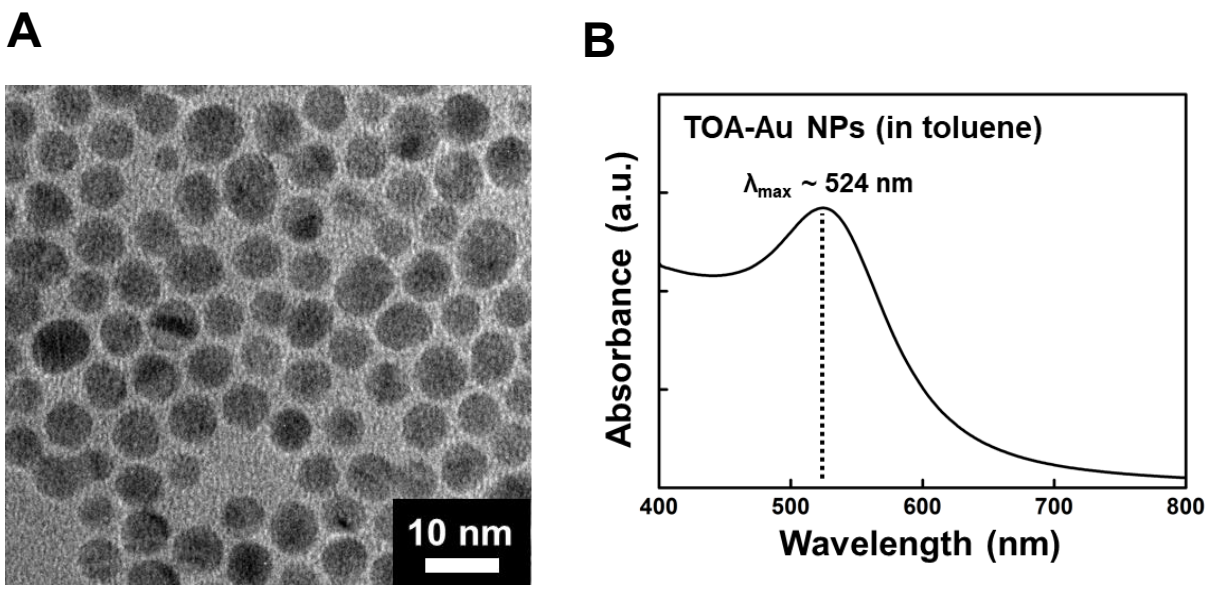

Figure S4. Characterization of synthesized TOA-Au NPs. High-resolution TEM image of TOA-Au NPs with a diameter of 8 nm (**A**) and UV-Vis spectra of TOA-Au NPs dispersed in toluene (**B**).

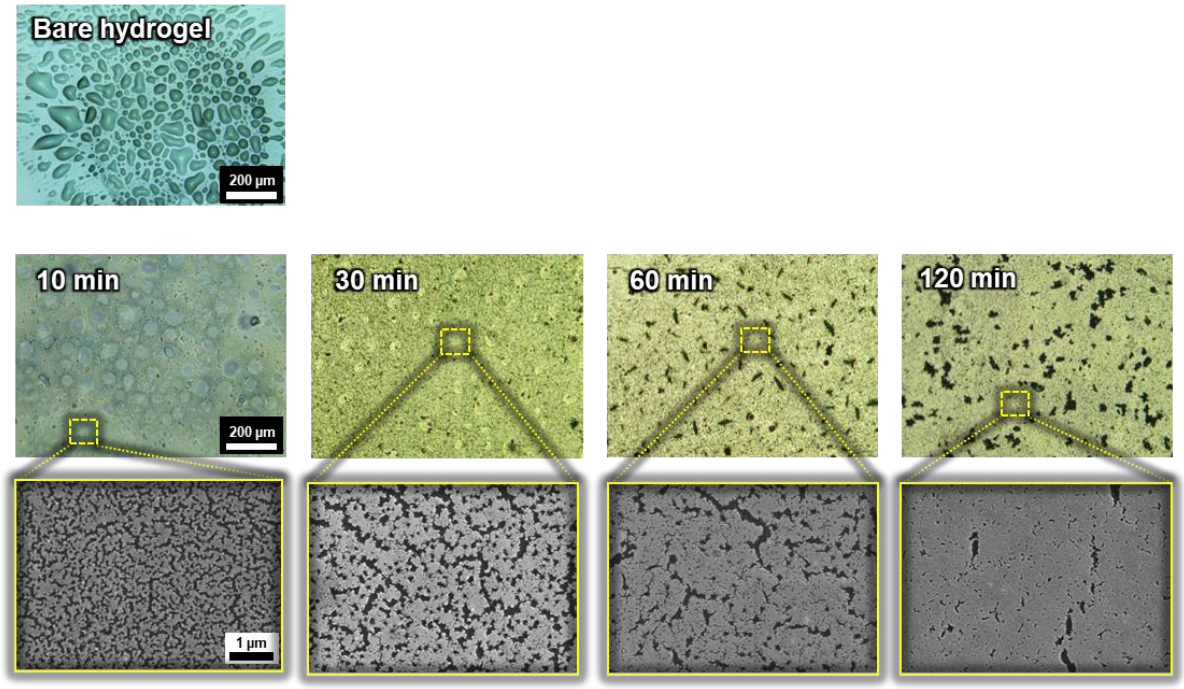

Figure S5. Capillary-assisted *in situ* NP assembly. Optical and SEM images of capillary-assisted *in situ* NP assembly on the surface of hydrogels with increasing assembly time to 120 minutes.

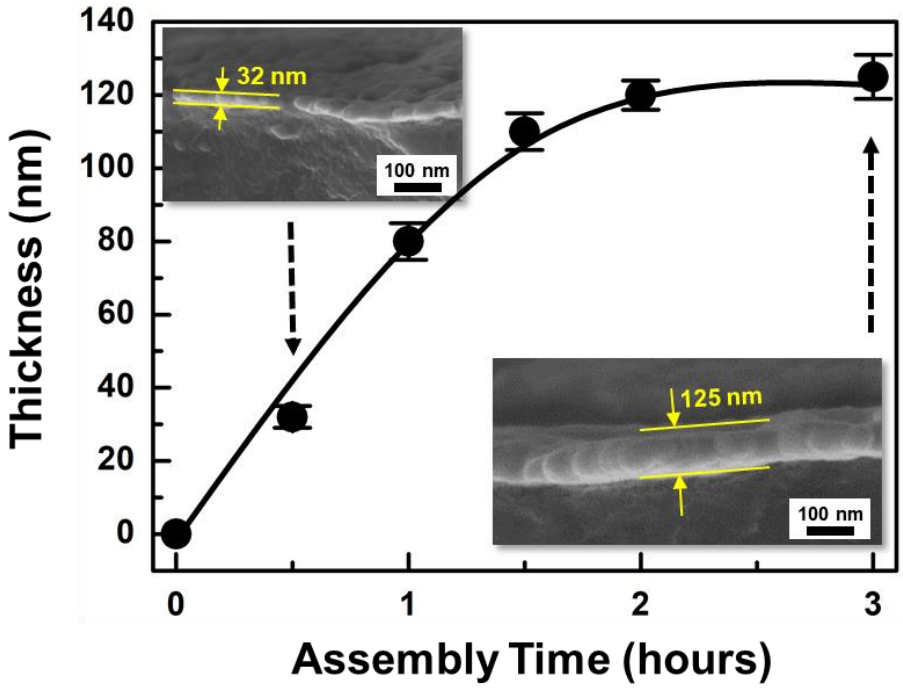

Figure S6. Capillary-assisted *in situ* NP assembly. Thickness of capillary-assisted *in situ* NP assembled metallic layers on hydrogels as a function of assembly time.

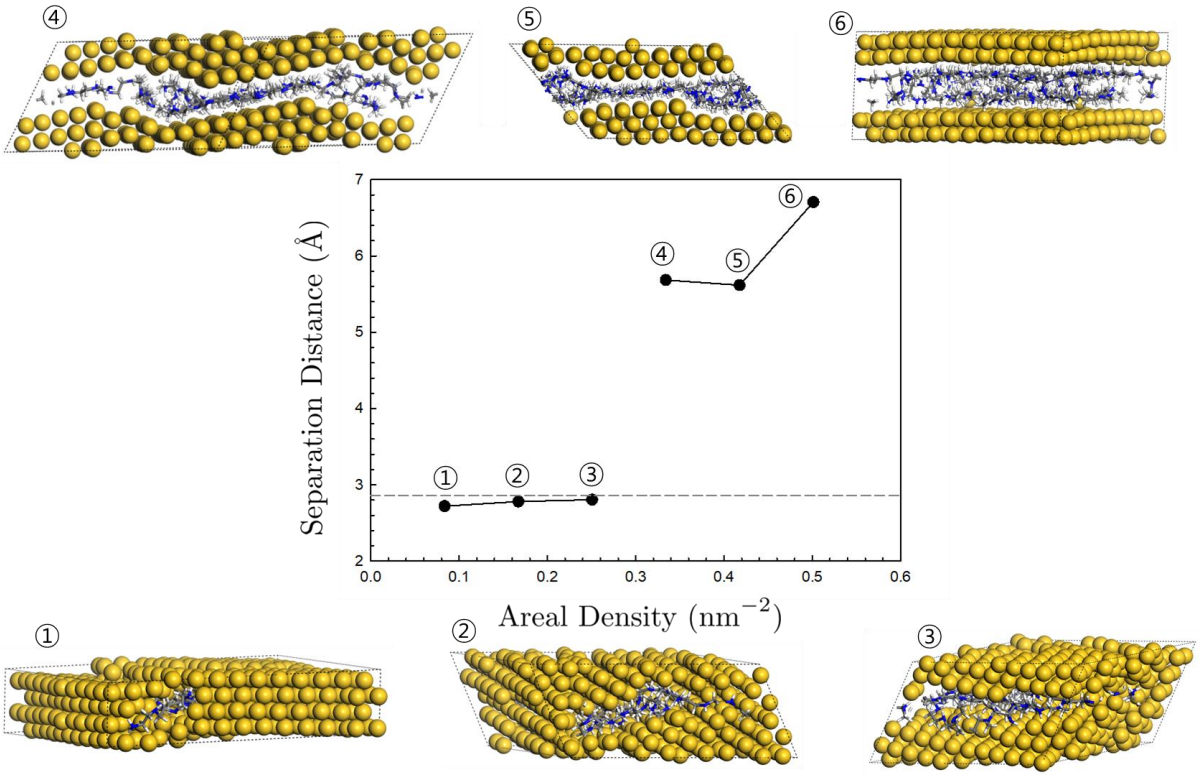

Figure S7. Conformations of PEI adsorbed between AuNPs. The minimal seperation distance between Au (110) surfaces (separated by *n* PEI chains) as a function of areal density of PEI chains on Au surface. In this case, the areaial density is defined as the number of PEI chains per the initial area of Au surface. The grey dashed line represents the value of Au-Au distance in the bulk lattice (2.884 Å), implying the formation of the metallic sintering between initially separated two Au slabs. The numbered images show the molecular structures simulated at the corresponding data points.

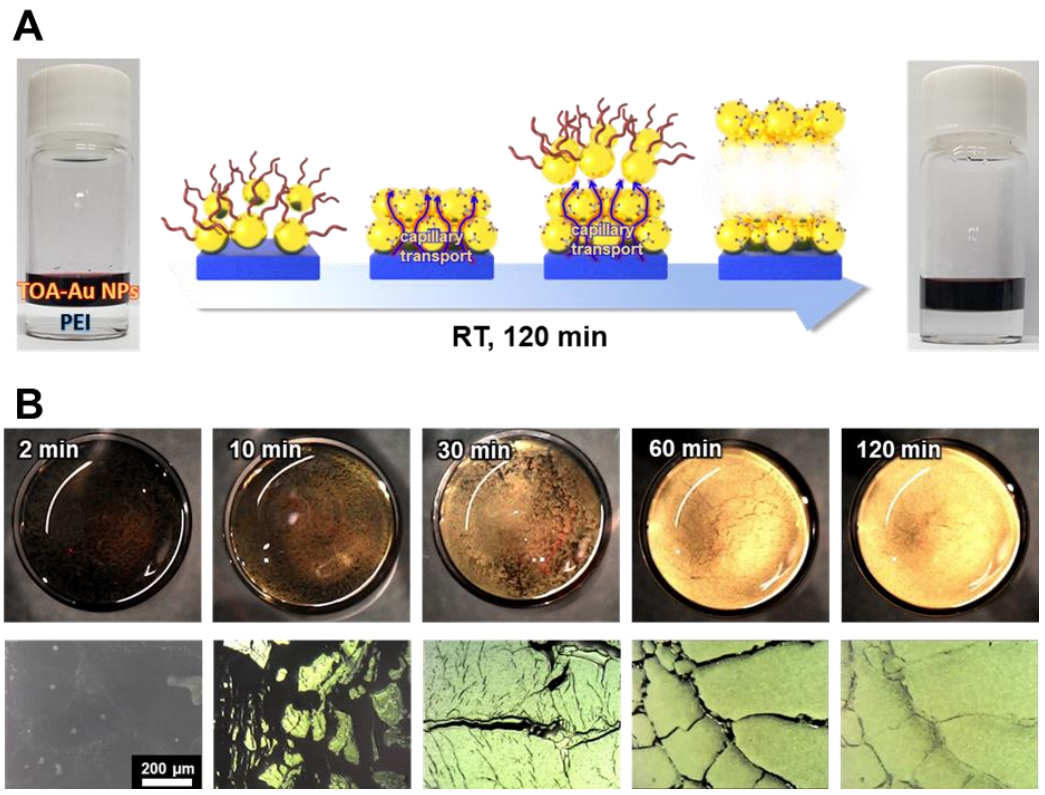

Figure S8. Capillary-assisted *in situ* NP assembly. Schematic illustration of capillary-assisted *in situ* nanoparticle assembly at the interface between TOA-Au NPs dispersed toluene phase and PEI dispersed aqueous phase (**A**). Capillary transport of PEI molecules from PEI aqueous solution through porous NP-assembled structured leads to continuous ligand exchange reaction with TOA ligands and room-temperature sintering of adjacent nanoparticles. Photographic and optical microscopic images measured from bottom of the vials with increasing assembly time up to 120 minutes (**B**).

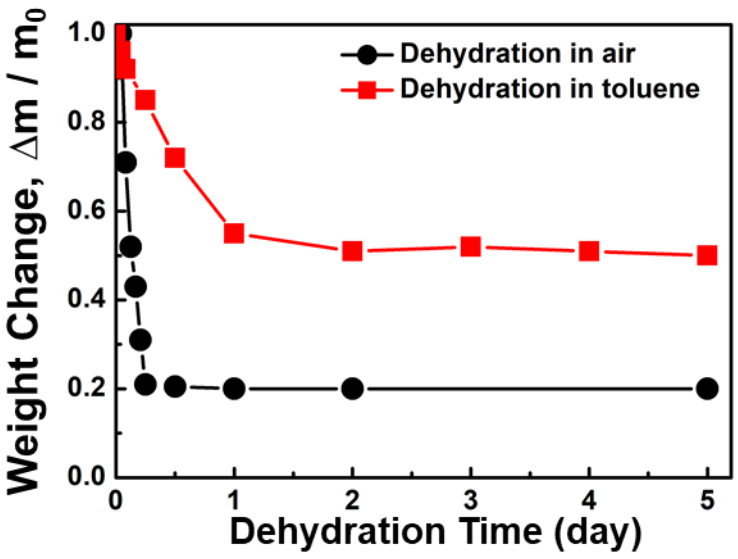

Figure S9. Deswelling of WNE-coated PAA-co-PAAm hydrogels. Weight changes of Au nanomembrane electrode-coated PAA-co-PAAm hydrogels as a function of dehydration time in air or toluene.

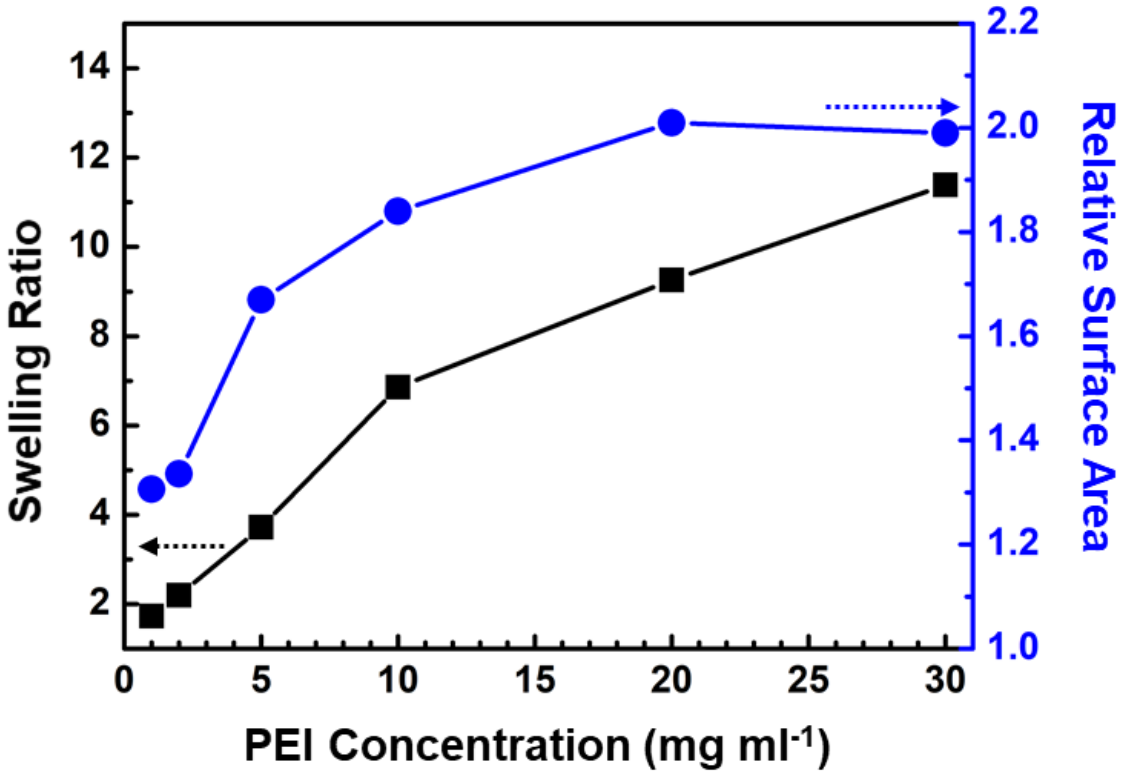

Figure S10. PEI concentration-dependent properties. PEI concentration-dependent swelling ratio of PAA-co-PAAm hydrogel and relative surface area of wrinkled nanamembrane electrode coated on PAA-co-PAAm hydrogels.

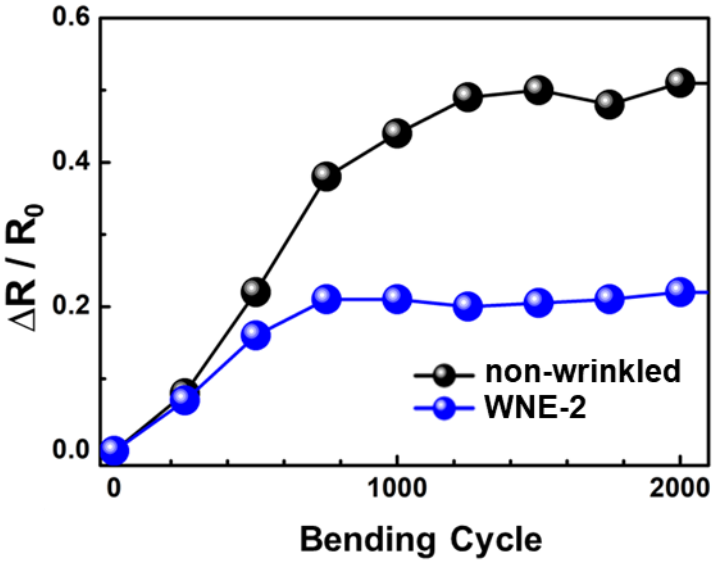

Figure S11. Mechanical stability of WNE-hydrogels. Mechanical stability tests for the Au-nanomembrane electrode (non-wrinkled) and wrinkled electrode with relative surface area of 2 (WNE-2) coated on PAA-co-PAAm hydrogels as a function of the bending cycling number

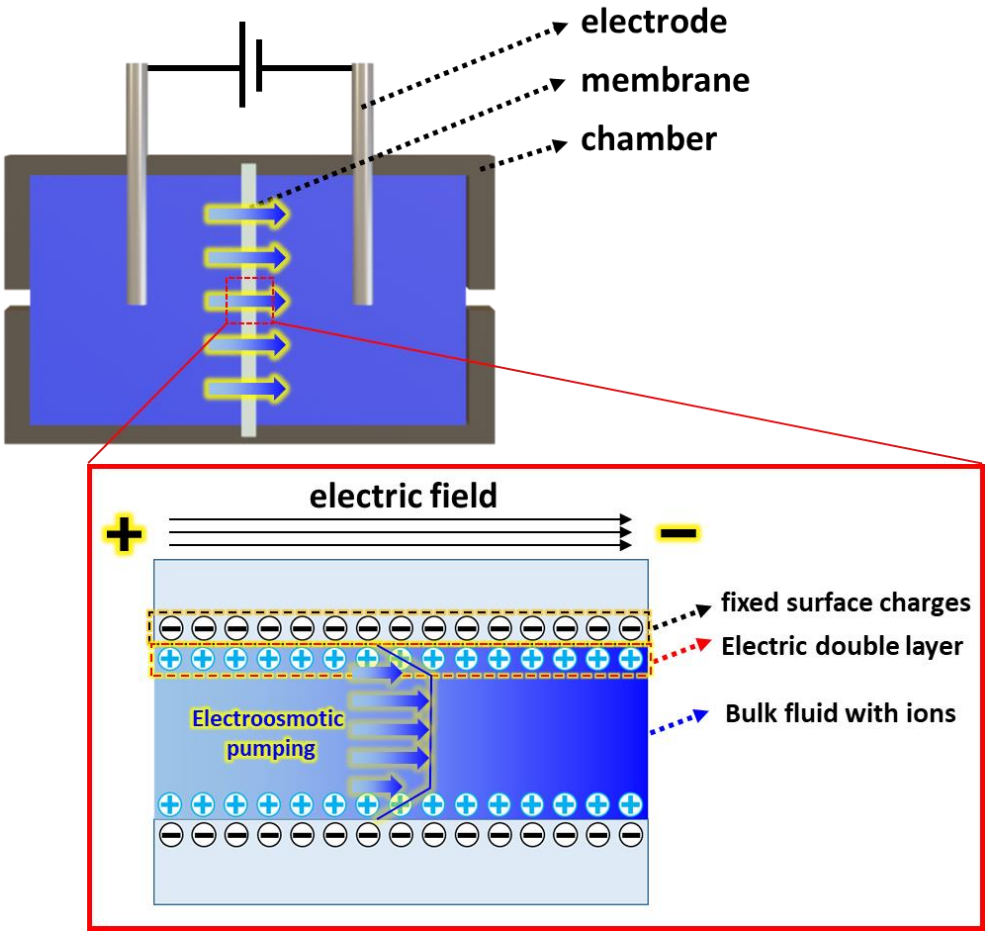

Figure S12. Schematic illustration of conventional electroosmosis device with working mechanism. Electroosmosis is a macroscopic electrokinetic phenomenon, which generate the flow of liquid electrolyte (ionic fluid) through a microporous medium by the applied electric field. When the liquid electrolyte contacts with microporous membrane with fixed surfaces charges, electric double layers are induced. Applied electric field attracts the electric double layers in microchannel, which consequently result in the net movement of bulk fluid.

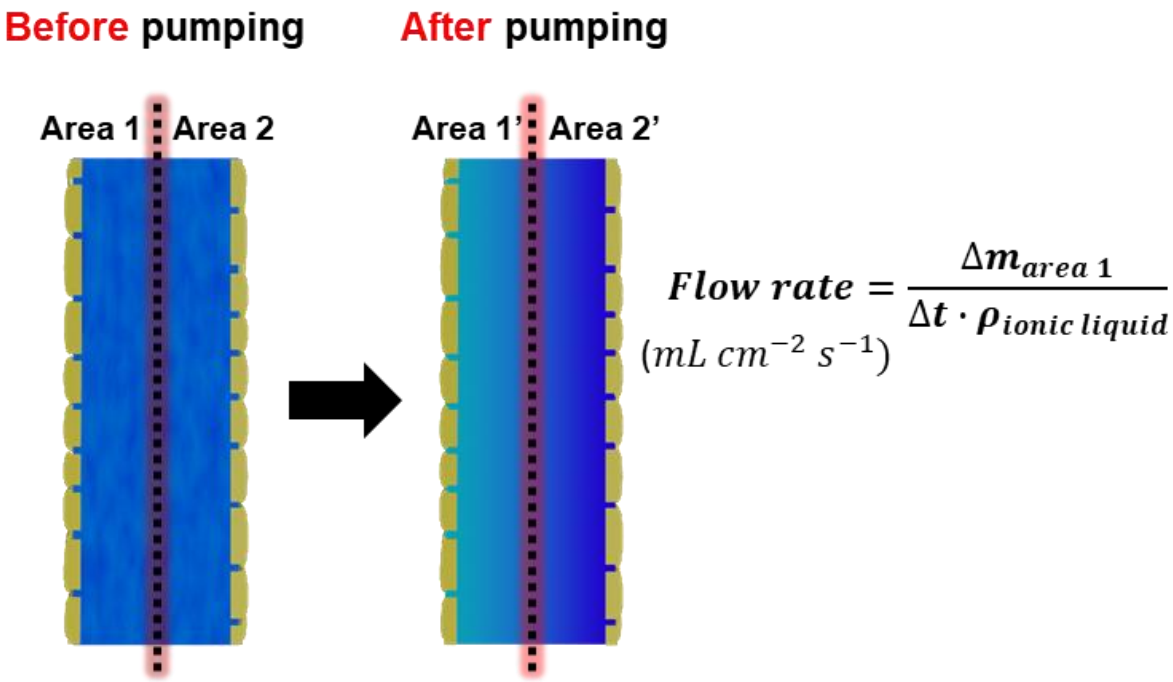

Figure S13. Schematic illustration of quantitative characterization of electroosmosis pumping of WNE-coated hydrogels. For quantitative characterization, we prepared the half-cut thick hydrogel devices (> 2 mm) and measured the mass changes of each pieces before and after applying electric potential. Based on this method, we roughly estimated actual amount of pumped liquid inside hydrogel as a function of applied time under constant electric potentials.

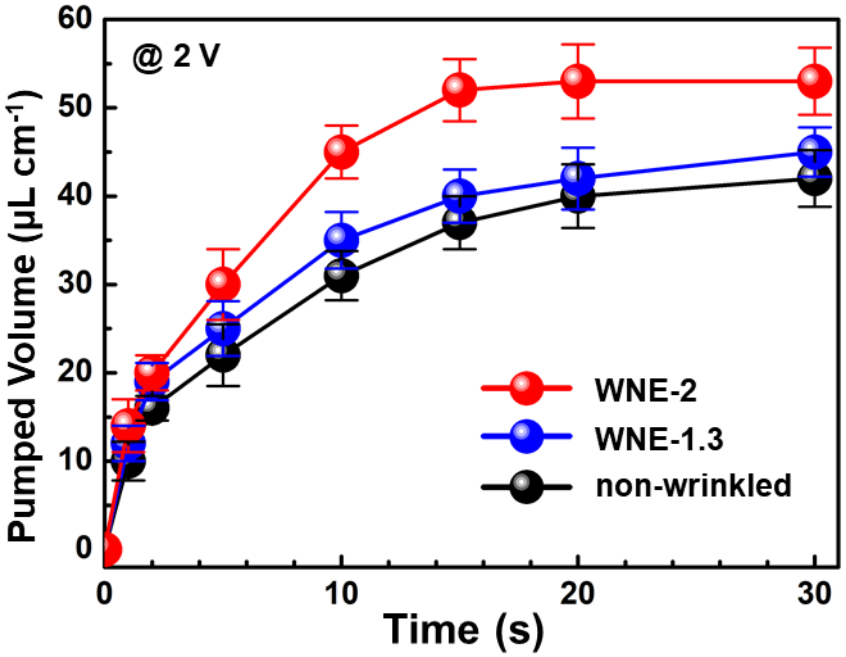

Figure S14. Effect of surface area of wrinkled electrode. Electroosmotic pumped volume of WNE-coated PAA-co-PAAm with different surface area of wrinkled electrodes.

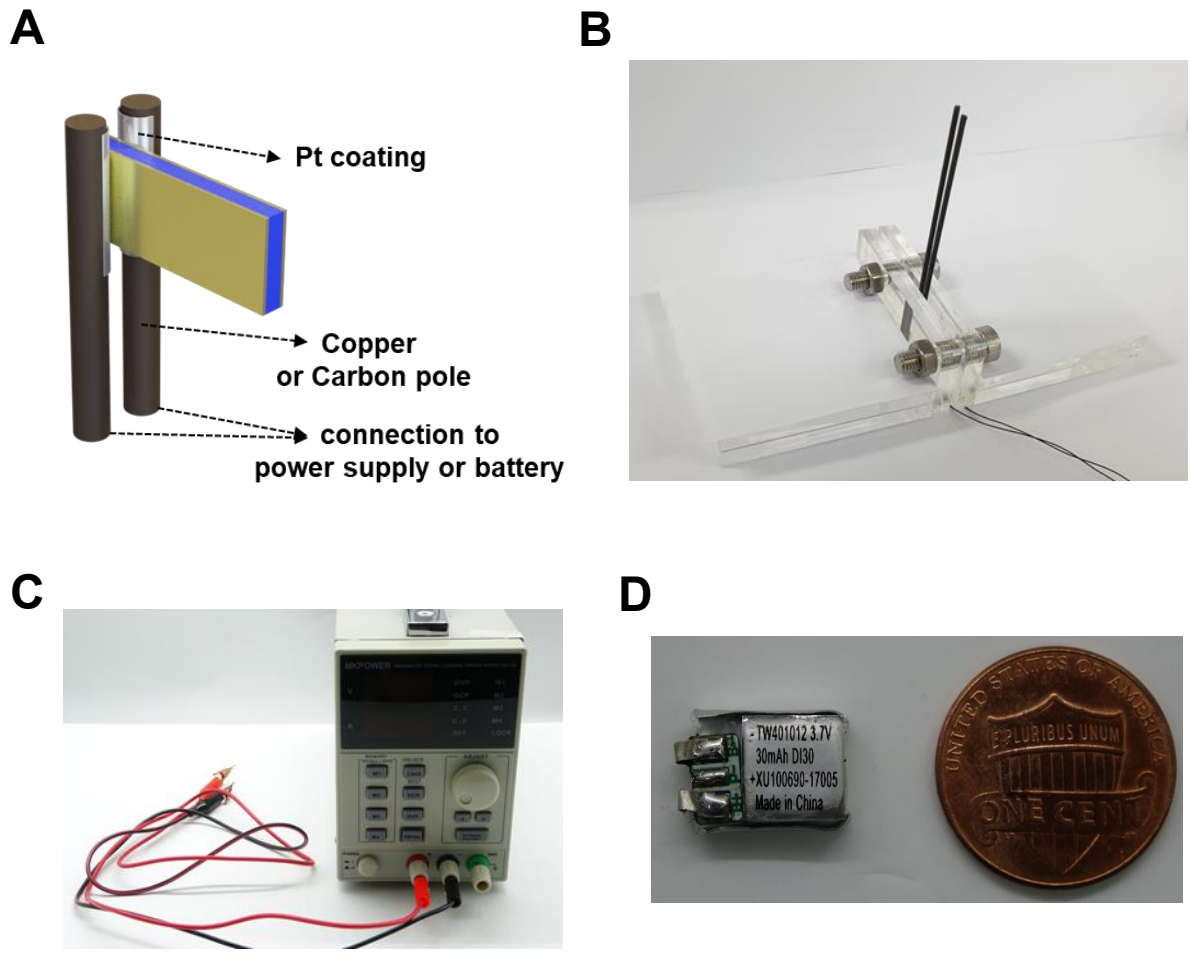

Figure S15. Experimental setup. Schematic illustration of experimental setup for WNE-actuators (**A**) and photographic images of sample stage (**B**), power supply (**C**), and battery (**D**). Carbon pole with a diameter of 1 mm (or Pt-coated copper pole with a diameter of 2 mm) was used for applying an electric potential to actuators in order to minimize the mechanical and electrochemical damages of WNE-actuators during the operation.

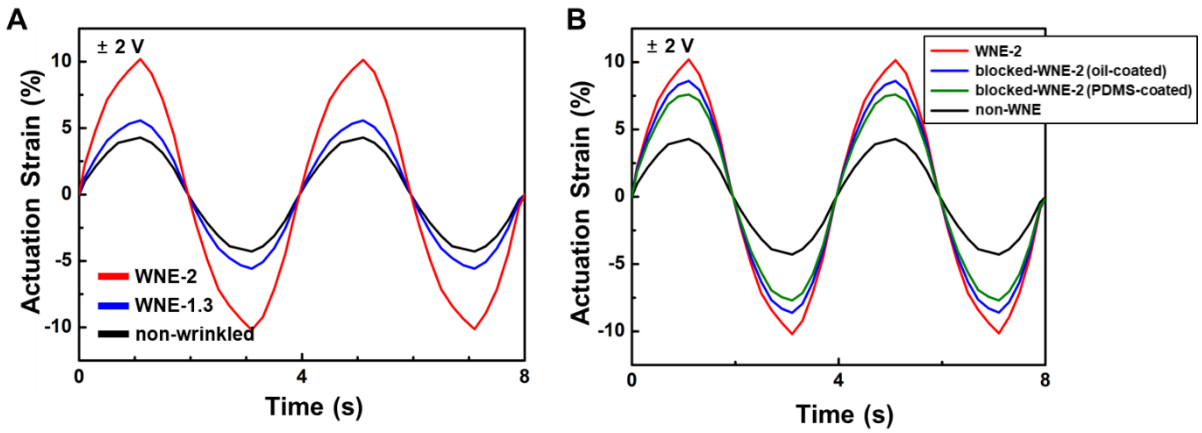

Figure S16. Importance of morphologies of wrinkled nanomembrane electrodes. Actuation strain of non-wrinkled, WNE-1.3, and WNE-2 based 450-μm-thick hydrogel actuators operated at 2 V (frequency of 0.25 Hz) (**A**). Actuation strain of WNE-2, non-WNE, and WNE-2 blocked by oil and PDMS coated 450-μm-thick hydrogel actuators operated at 2 V (frequency of 0.25 Hz). (**B**).

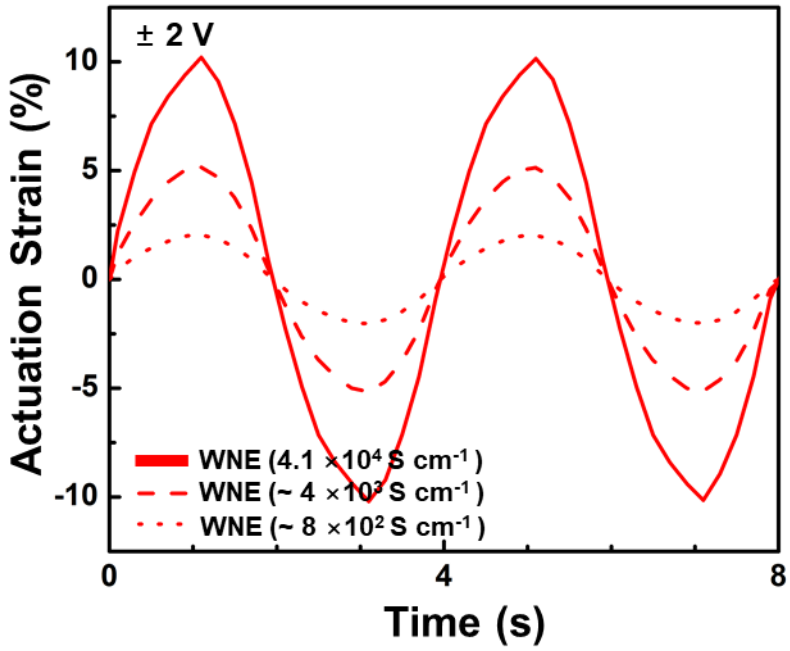

Figure S17. Effect of electrical conductivities of WNE actuator. Actuation strain of WNE-2 with different electrical conductivities based on 450-μm-thick hydrogel actuators operated at 2 V (frequency of 0.25 Hz).

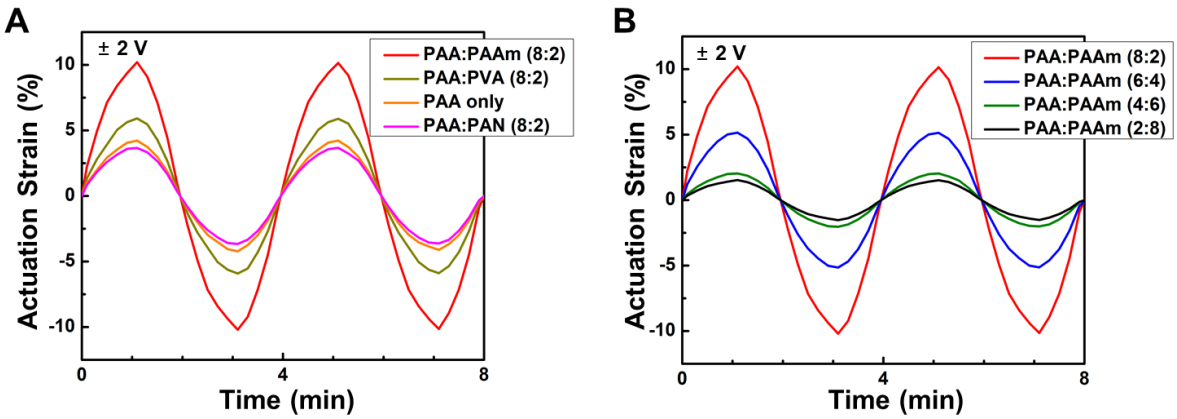

Figure S18. Effect of hydrogel composition on actuation performance. Actuation strain of WNE-coated acrylic acid-based hydrogels (**A**), and PAA-co-PAAm with different composition ratio (**B**) based on the 450 μm-thick hydrogel actuators operated at 2 V (frequency of 0.25 Hz).

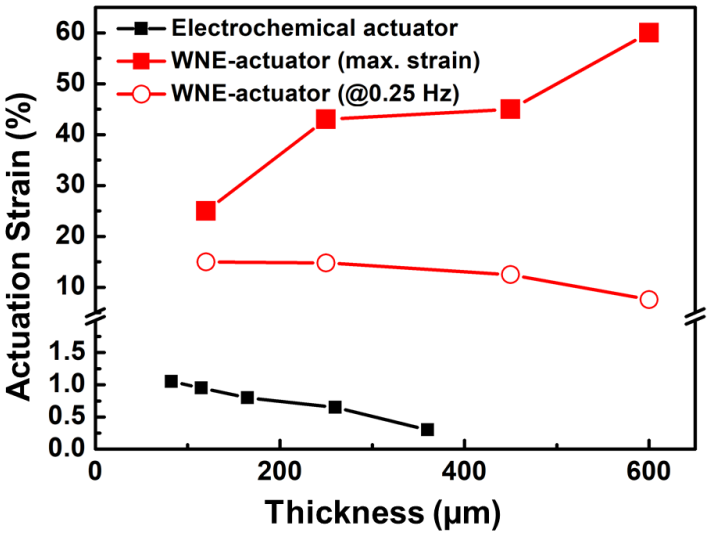

Figure S19. Comparison with electrochemical actuator. Actuation strain (measured at 0.25 Hz of AC voltage and maximum condition) of electrochemical actuator and WNE-actuator as a function of thickness. Thickness-dependent actuation strains of electrochemical actuator were obtained from Umrao, S. et al. *Sci. Robot.* **4**, eaaw7797 (2019) [*33*].

Table S1. Comparison of actuator performances.

Type of actuator	Strain (%)	Energy density (kJ m^{-3})	Power density (kW m^{-3})	Specific power density (W kg^{-1})	Driving voltage (V)	Efficiency (%)	ref
Skeletal muscle	20-40	8-40	50-300	50-300	-	40	(*7, 69*)
Pneumatic actuator	10-40	1-200	10-1000	> 10^4	-	11 – 33	(*7, 69, 70*)
Shape-memory alloy	4-8	10^4-10^5	10^3-10^5	< 5 x10^4	1–10 (< 1 V/mm)	< 5	(*7, 69, 71*)
Dielectric elastomer actuator	1-1000	100-500	10^3-10^5	750-3400	> 1000	25 – 90	(*7, 69, 72*)
Electrochemical actuator (IPMC or carboneous electrodeionc polymer composite)	< 2	1-65	0.01-30	0.01-20	2-7	< 7.5	(*29-33, 36, 69*)
This work	**60**	**750**	**38**	**33**	**1.5-3**	**22.8**	

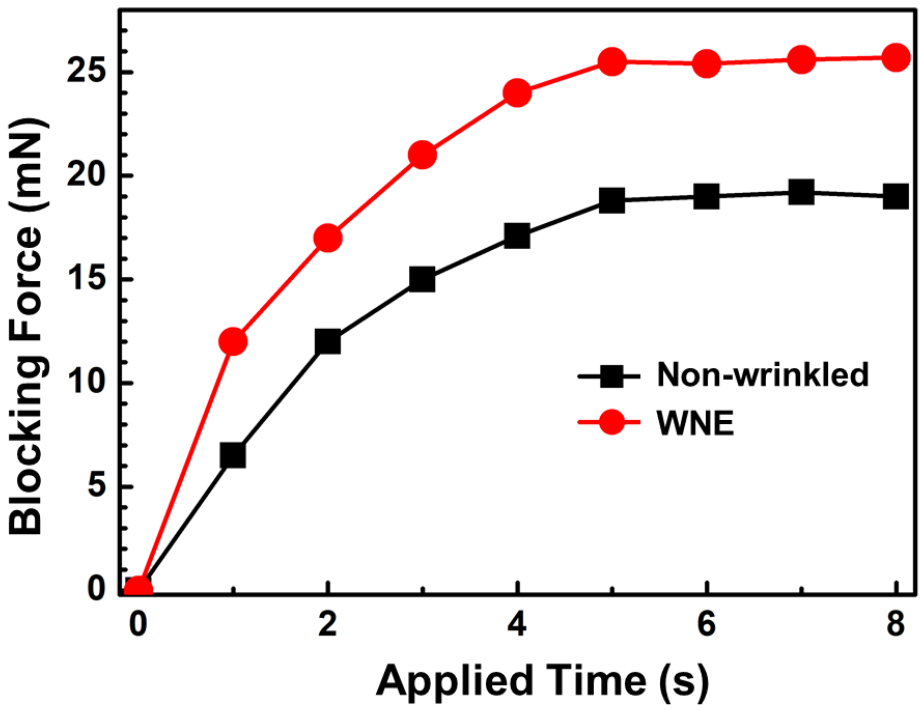

Figure S20. Blocking forces of WNE-actuators. Maximum blocking forces of WNE-actuators (2 cm x 0.7 cm x 450 µm, 72 mg) operated at 3 V as function of individually accumulated applied time.

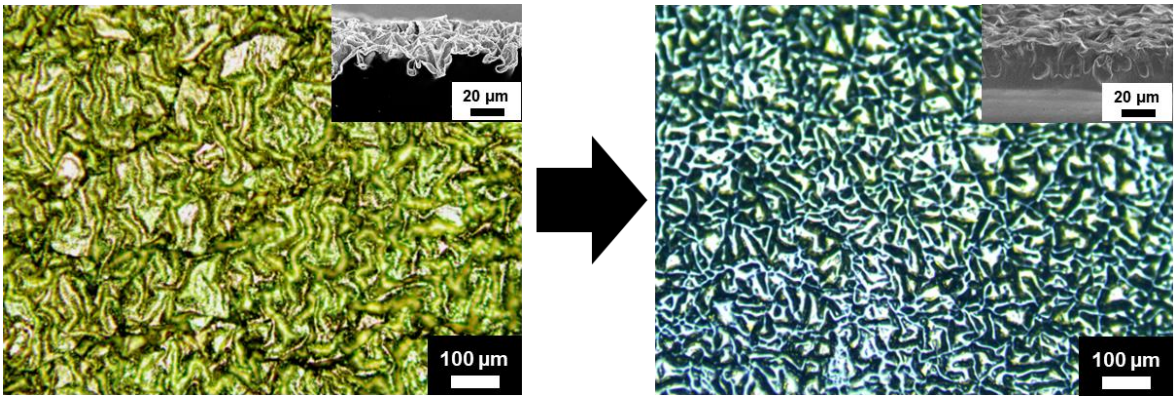

Figure S21. Encapsulation layers on WNE-actuators. Optical microscopy images and cross-sectional SEM images (inset) of WNE-actuators before and after PDMS coatings.

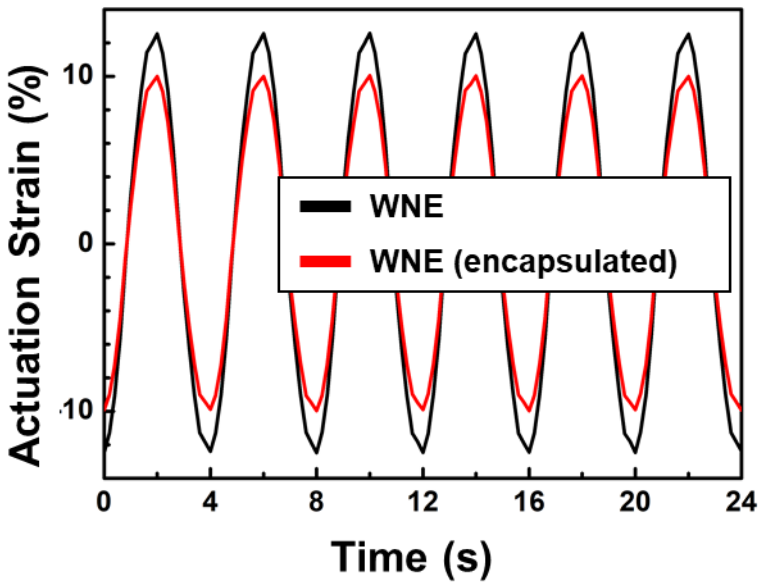

Figure S22. Effect of encapsulation layer. Actuation strain of bare and encapsulated 450-µm-thick WNE-actuators operated at 3 V (0.25 Hz).

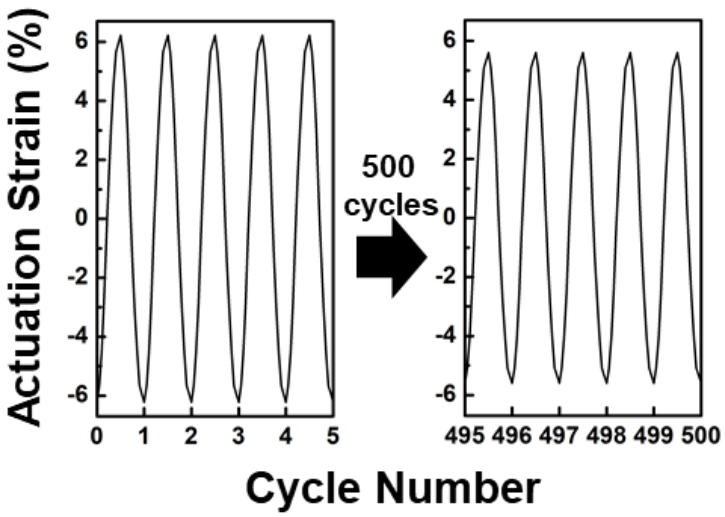

Figure S23. Operation stability of WNE-actuators. Operation stability of PDMS-coated 450-μm-thick WNE-actuators operated at 2 V (1 Hz).

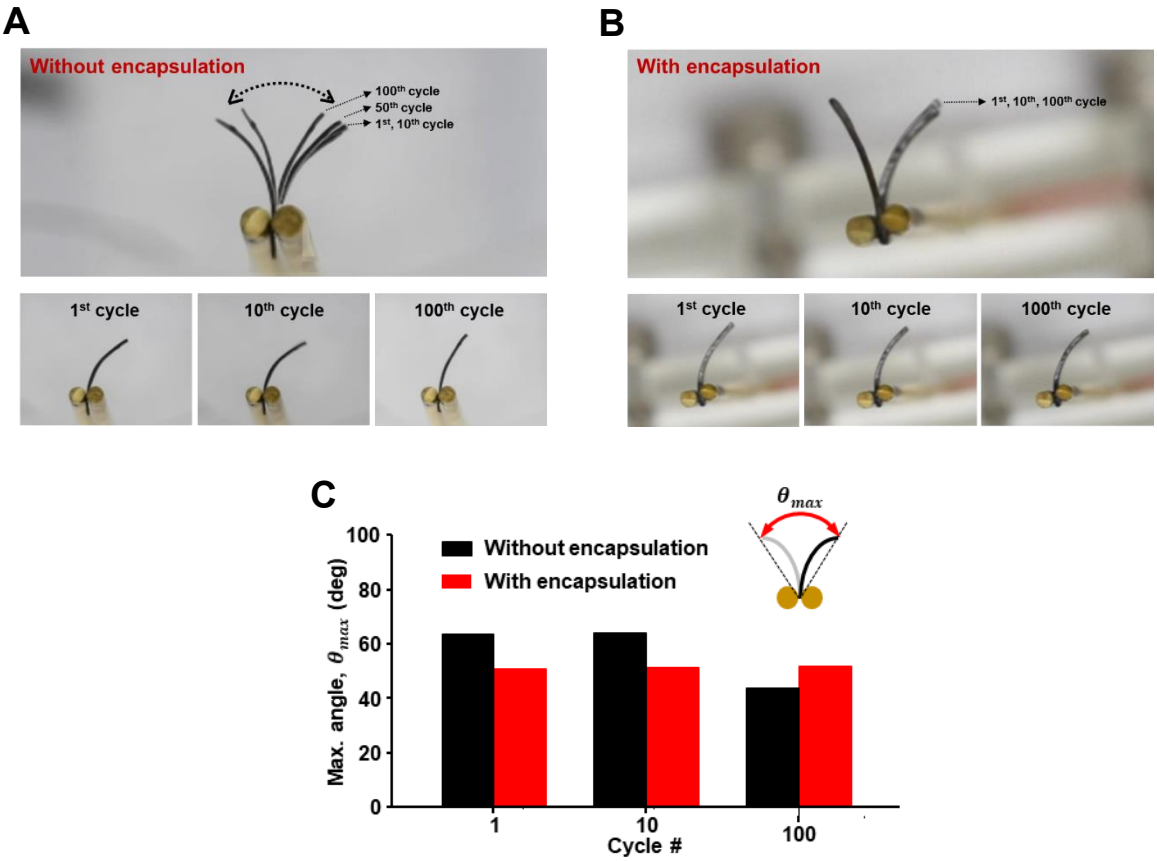

Figure S24. Repeatable actuating motions. Photographic overlay images of WNE-actuators at 1st, 10th, and 100th cycle (2.5 V, 1 Hz) without (**A**) and with (**B**) encapsulation layer. Maximum angle of WNE-actuator with and without encapsulation layer under different cyclic actuation (**C**).

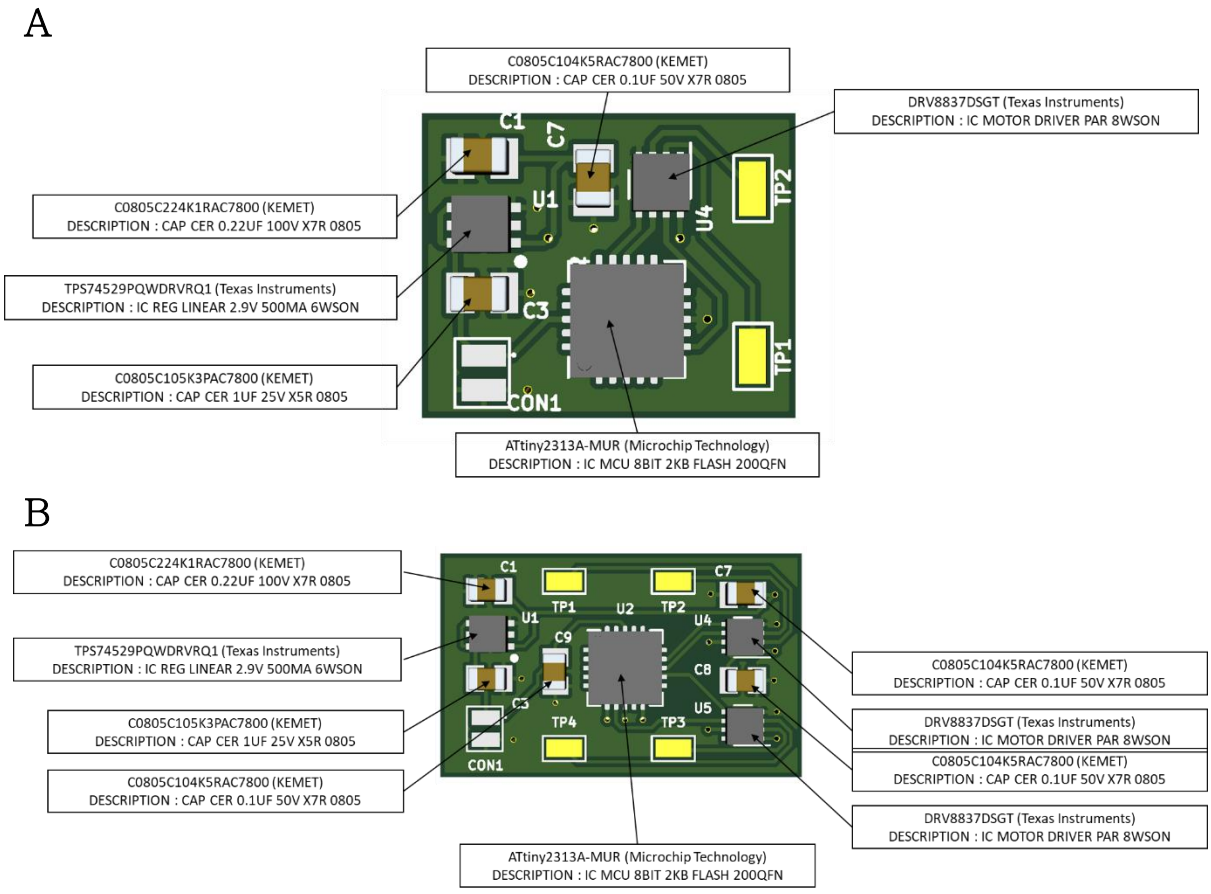

Figure S25. Circuit boards for aquabots. Schematic illustration and description of circuit boards used for flapping aquabots (**A**) and sculling aquabot (**B**).

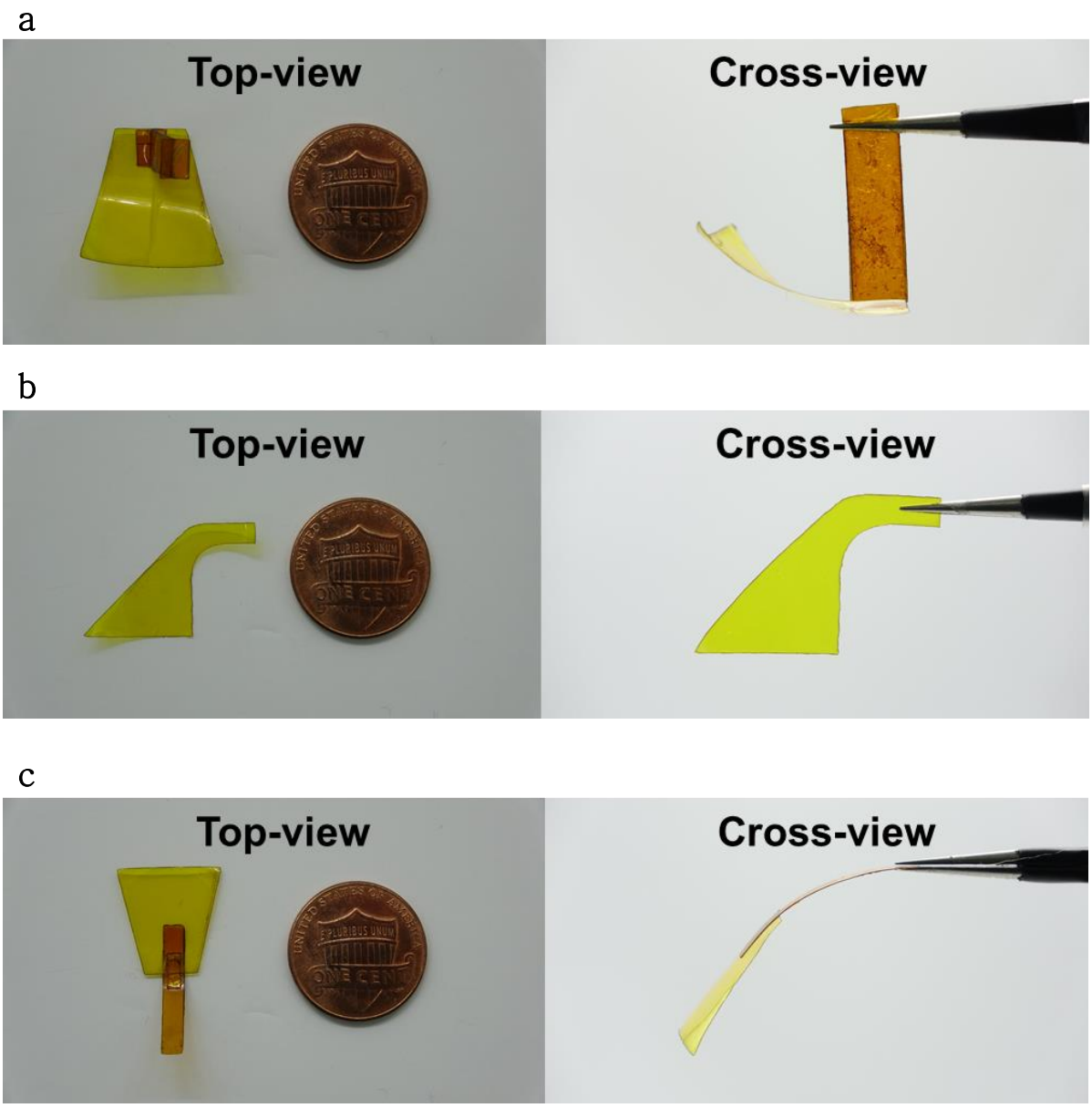

Figure S26. Fins for aquabots. Photographic images of fins used for flapping (up-down) (**A**), flapping (left-right) (**B**), and sculling motions (**C**).

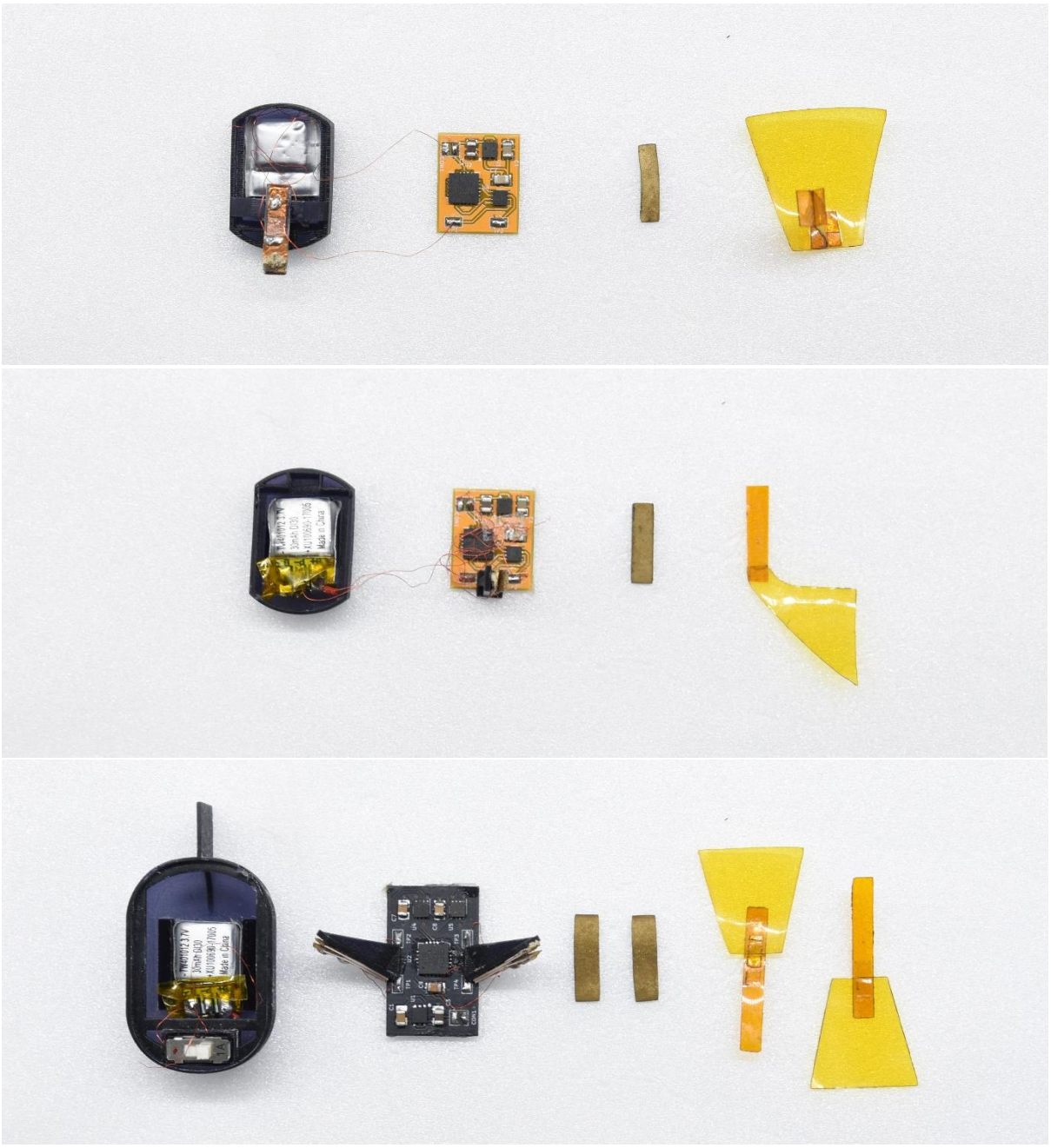

Figure S27. Aquabots with flapping and sculling motions. Photographic images of aquabots composed of robot body, battery, circuit board, fins and WNE-actuators.

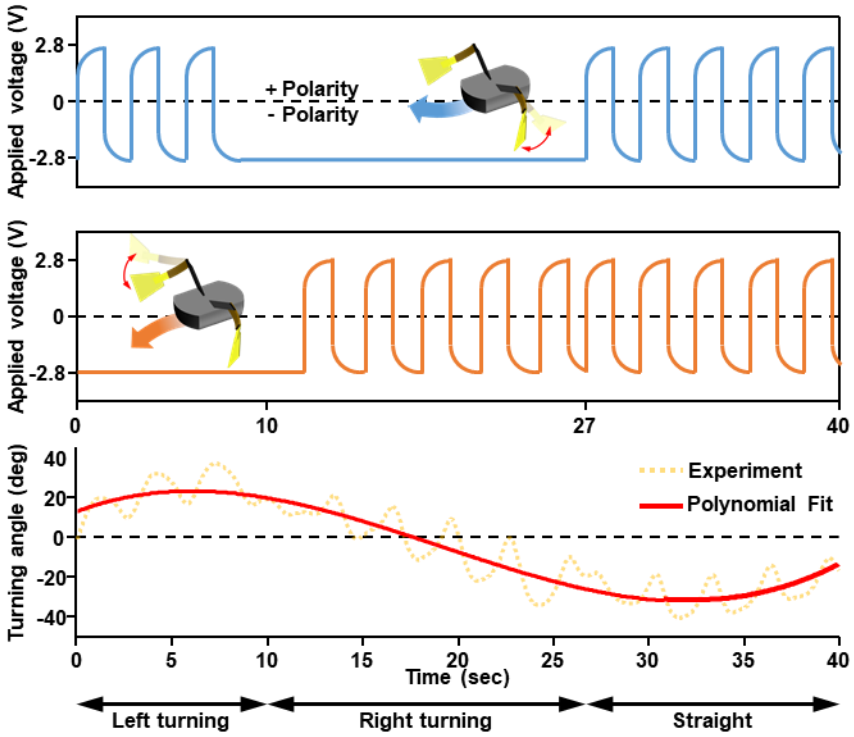

Figure S28. Maneuvering test of the aquabot with a feed forward command. Applied voltages and turning angle of the aquabot as a function of time showing controllability of WNE-actuators based aquabots.

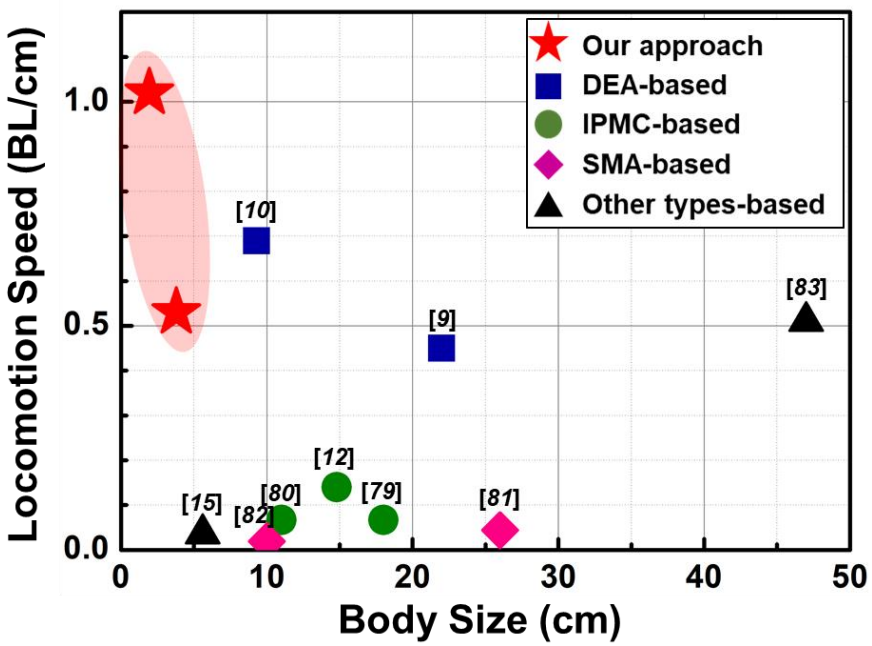

Figure S29. Performance of WNE-actuator based aquabots. Performance comparison between WNE-actuator-driven soft aquabots and previously reported untethered soft aquabots driven by DEA, SMA, and IPMC.

Table S2. Comparison of aquabots based on different types of soft actuators.

Actuation system	Robot	Body length (cm)	Weight (g)	Max. velocity (BL/s)	Electric driving input	Actuator	Ref.
Tethered	Swimming robot	10	14.3	0.77	4800 V	DEA	*(73)*
	FEDEA	22	-	0.009	7500 V	DEA	*(11)*
	Soft Biomimetic fish robot	15	4.4	0.25	5000 V	DEA	*(74)*
	Biomimetic robotic swimmer	8.75	5.05	0.526	3 V	IPMC	*(75)*
	Soft robotic fish	19.5*	-	0.15	50 V	SMA	*(76)*
	Stingray-inspired soft swimmer	23.6*	-	0.2	3.3 A	SMA	*(41)*
	Micro-robotic fish	6	1.93	0.75	130 V	PZT	*(77)*
	Median-finned robot	58	-	0.61	-	FEA	*(78)*
Untethered	Electro-ionic fish†	9.3	90.3	0.69	9500 V	DEA	*(10)*
	Snailfish robot†	22	-	0.45	8000 V	DEA	*(9)*
	Robotic fish	14.8	140	0.14*	3.3 V	IPMC	*(12)*
	Soft robotic fish 2	18	290	0.067	7.3 V	IPMC	*(79)*
	Robotic manta ray	11	-	0.067	4 V	IPMC	*(80)*
	Turtle robot†	26	588	0.044	0.75 A	SMA	*(81)*
	Soft robotic fish 3	10	-	0.019	3.3 V	SMA	*(82)*
	Bionic robotic fish	5.6*	-	0.036*	3.7 V	LMAM	*(15)*
	SoFi†	47	1600	0.51	32.8 V	FEA	*(83)*
	This work – flapping	**1.95**	**1.47**	**1.02**	**2.8 V**	**Electroosmotic hydrogel**	
	This work - sculling†	**3.5**	**2.51**	**0.53**	**2.8 V**		

*values estimated from references; †feedforward control; Dielectric elastomer actuator (DEA); Liquid metal artificial muscle (LMAM); Ionic polymer-metal composite (IPMC); Shape memory alloy actuator (SMA); Fluidic elastomer actuator (FEA); Piezoelectric actuator (PZT)

Other Supplementary Material

Movie S1. Electroosmosis pumping of WNE-coated hydrogels. When an external electric field (2 V and 3V) is applied to WNE-coated hydrogel, ionic fluid was reversibly induced with different frequencies from 0.5 Hz to 0.125 Hz.

Movie S2. Actuation of WNE-coated hydrogel actuators. Bending motion of 450-μm-thick WNE-actuator by applying ± 2 and 3 V with different frequencies from 0.25 Hz to 2 Hz.

Movie S3. Battery-powered WNE-coated hydrogel actuators. WNE-actuator is operated with on-board electronics and a small battery. The actuation of a small battery-powered WNE-actuator is consistent with the actuation strain of WNE-actuator operated with an external power source.

Movie S4. Demonstration of untethered soft aquabots. Untethered soft aquabots based on WNE-actuators with flapping motion (body size: 1.95 cm) and sculling motion (body size: 3.8 cm) are demonstrated. The WNE-actuator occupied just 2% of the body mass, but its power density is power density is high enough to generation a maximum speed of 1.02 BL s^{-1}.

Movie S5. Maneuvering of untethered soft aquabot. Maneuvering of untethered soft aquabots with sculling motion (body size: 3.8 cm) is demonstrated. By controlling the two actuators with a programed control signal at alternating 2.8 V potential, it is demonstrated that the aquabot can be steered and make forward movements for maneuvering.